Article

Laser Textured Superhydrophobic SiC Ceramic Surface and the Performance of Condensation Heat Transfer

Deyuan Lou [1], Gengxin Lu [1], Heng Li [1], Pengjian Chen [1], Qing Tao [2], Qibiao Yang [2] and Dun Liu [1,*]

[1] Laser Group, School of Mechanical Engineering, Hubei University of Technology, Wuhan 430068, China; loudeyuan@hbut.edu.cn (D.L.); m13995934081@163.com (G.L.); 15926338563@163.com (H.L.); cpg389246@163.com (P.C.)

[2] Hubei Provincial Key Laboratory of Green Materials for Light Industry, Hubei University of Technology, Wuhan 430068, China; taoqing107@aliyun.com (Q.T.); yangqibiao@hbut.edu.cn (Q.Y.)

* Correspondence: dun.liu@hbut.edu.cn

Abstract: Chemical modification is usually utilized for preparing superhydrophobic SiC surfaces, which has the problems of long processing time, high environmental contamination risk, and high cost. To enhance the condensation heat transfer efficiency of SiC, the superhydrophobic SiC surface was fabricated through laser texturing and heat treatment. In this study, the SiC surface was processed by laser texturing with a nanosecond laser, followed by heat treatment. Surface microstructures and compositions were investigated with SEM and XPS, and the heat transfer coefficient of the superhydrophobic SiC surface was tested. The results indicated that the laser-textured SiC surface had a super hydrophilic contact angle of $0°$; after heat treatment, SiC ceramic became superhydrophobic (surface contact angle reaches $164°$) because organic contamination on the original SiC surface could be cleaned by using laser texturing, which caused a chemical reaction and the formation of SiO_2 on the surface. Moreover, the distribution of relatively low-energy SiO_X was formed after heat treatment; then, SiC ceramic became superhydrophobic. Due to the formation of nanoscale sheet-like protrusion structures by heat treatment, the SiC superhydrophobic surface exhibited typical dropwise condensation, and the condensation heat transfer coefficient reached $331.8 \, W/(m^2 \cdot K)$, which was 2.3 times higher than that of the original surface.

Keywords: SiC; laser texturing; superhydrophobic; dropwise condensation

1. Introduction

SiC has the advantages of excellent hardness [1], chemical stability, good wear resistance, good thermal conductivity, a wide forbidden band, and a low coefficient of thermal expansion. Nowadays, as power devices produce more and more heat, a system has a higher and higher requirement for heat dissipation from the substrate. Since the substrate for high-power devices is often ceramic, in order to solve the heat dissipation problem of power devices, an integrated micro heat pipe is proposed to embed in SiC substrate [2–4]. More brightness, lower cost, less energy consumption, a longer life span, and a smaller unit chip area are all advantages of LEDs using SiC ceramic substrates.

Condensation heat transfer has significant application potential and industrial value because it is widely employed in many industries, including power generation, the chemical industry, saltwater desalination, microelectronics, aviation, and others [5–7]. Two common forms of condensation are filmwise condensation and dropwise condensation. Filmwise condensation is a process in which water vapor spreads into a film on the cooling wall surface, wets the wall surface, and condenses into a liquid film. Drop condensation form: condensation cannot be spread on the surface, forming a small liquid droplet, showing a drop shape. Dropwise condensation, as a type of effective condensation heat transfer, is several times or even ten times higher than the heat transfer coefficient of filmwise condensation [7].

In practice, superhydrophobic (SHPo)/hydrophobic surfaces are necessary for dropwise condensation [8]. Methods for the preparation of SHPo surfaces include chemical etching [9,10], self-assembly technology [11,12], coating technologies [13–15], and mechanical processing [16]. Preston et al. [15] produced graphene coatings on copper tubes using an ultrathin scalable chemical vapor deposition technique. The outcomes demonstrate that the graphene coating effectively promotes dropwise condensation while providing strong chemical stability and maintaining low thermal resistance. The heat transfer performance was improved by a factor of 4 compared to pristine copper tubes. The relatively low forward and backward contact angles of graphene compared to fluoropolymer coatings make it less likely to induce superhydrophobic behavior on micro/nanostructured materials. Lv et al. [13] used a two-step technique to manufacture superhydrophobic PTFE/CuO coatings on aluminum plates with contact angles larger than 150° and water-sloshing angles less than 10°. The outcomes demonstrate that 6061Al substrates can be shielded from corrosion and contamination by PTFE/CuO coatings. In addition, the PTFE/CuO samples remained superhydrophobic after UV, thermal, and mechanical stability tests, indicating that the 6061Al substrates with PTFE/Cu coatings can be applied under harsh conditions. These methods have long processing times and can bring pollution to the environment. Laser processing, as a new and green processing method [17], has the following advantages: (1) controllable process and easy-to-realize industrial applications; (2) high processing efficiency and speed, without the need to add a coating layer on the material surface, thus greatly improving the processing efficiency; (3) low cost and pollution-free, without additional chemicals. Therefore, laser processing is widely used in preparing superhydrophobic surfaces [18–20].

Chemical vapor infiltration technology is used to overcome the manufacturing of exceptional-tough CNT/SiC composites [21]. Additionally, the chemical etching method can be used to fabricate large-scale porous SiC, but the surface has to be functionalized with perfluorooctyl trichlorosilane to reduce the surface energy. Oxidation of SiC appears to affect the wettability transition [22]. The SHPo SiC surface can be formed through the metal coating and adsorption of organic pollutants on the surface [14]. Superhydrophobicity can also be obtained by surface deposition of perfluoro silane [23]. Liu et al. [9] used a composite chemical etching method to prepare superhydrophobic SiC surfaces. The results showed that the surface roughness is significantly increased by composite etching compared to metal-assisted etching or reactive ion etching only. The porous SiC surface was functionalized with perfluorooctyl trichlorosilane, resulting in a superhydrophobic SiC surface with a contact angle of 169.2°. The superhydrophobicity of the SiC surface exhibited good stability at 85 °C and 85% humidity. Typically, it is very difficult to process the SHPo SiC surface. Furthermore, the aforementioned methods are not suited for green production due to their long processing time, high environmental contamination risk, and high cost.

In view of the shortcomings of the existing technology, this study analyzes the use of laser texturing (LT) technology in coordination with heat treatment (HT) technology to prepare SiC SHPo surface and realize surface dropwise condensation. This method has the advantages of a simple process, and zero chemical pollution, thus greatly improving the condensation heat transfer. It is a promising method for the condensation heat transfer of SiC ceramics or semiconductors.

2. Materials and Methods

2.1. Laser Texturing and Heat Treatment of SiC Surface

The experimental sample was SiC ceramic (SiC content 99.9 wt.%), size 50 mm × 50 mm × 4 mm. Before laser processing, SiC specimens were placed in the bottom of a clean beaker, 95% alcohol was added to submerge the specimens, then the beaker was placed in an ultrasonic cleaner (ultrasonic power 80 W) for 10 min. Then, the alcohol was poured into the waste water pool, and distilled water was added to the beaker to submerge the specimen. Then the beaker was placed in the ultrasonic cleaner again for

10 min, and the specimen was taken out to dry in the room to obtain the experimental SiC surface specimen.

The nanosecond fiber laser (SPI Lasers Ltd., UK), with a 100 W power, 0–240 ns pulse width, 1064 nm wavelength, 141 mm focal length, and 11 μm spot diameter, was selected. The parameters of scanning are shown in Table 1. The textured sample was put into an oven and maintained at 200 °C for 24 h. As there was no chemical reagent involved in the whole process, it was green processing. The experimental SiC samples in this work include three different samples: original, LT, and laser-textured and heat-treated (LT&HT) samples.

Table 1. The parameters of laser processing.

Wavelength [nm]	Pulse Width [ns]	Repeat Frequency [kHz]	Single Pulse Energy [mJ]	Scanning Speed [mm/s]
1064	145	160	0.4	1982

2.2. Characterization

The water contact angle of the sample surface was examined with a contact angle measuring instrument (MAIST Vision A-300, Ningbo Haishu Maishi Testing Technology Ltd., Ningbo, China). Each test was performed using deionized water and with a droplet volume of 6 μL. Each group of samples was measured three times, and the contact angles were averaged to avoid experimental chance. The surface morphology of the samples was subsequently observed with a field emission scanning electron microscope (FESEM, ZEISS GEMINI 300, Carl Zeiss AG, Jena, Germany). The test specimens were three SiC sample specimens, which were non-magnetic and met the equipment's environmental requirements. The scanning electron microscope was operated at a voltage of 3 kV. The 3D surface profile and surface roughness of the three different sample surfaces were measured using a 3D surface profiler (Contour GT-K, Beijing Yake Chenxu Technology Ltd., Beijing, China) made by Bruker. The surface composition was also analyzed using an X-ray photoelectron spectrometer (XPS, Thermos ESCALAB 250XI, Thermo Fisher Scientific, Waltham, MA, USA). The detection was performed with an Al target, and the physical phase analysis was performed with the X-ray photoelectron spectrometer in the 10 nm depth range of the surface layer of the specimen under the conditions of 100 μm beam diameter, scanning range 10–90°, step size 0.05°, speed 1 (°)/s, and resolution 0.48 eV, and finally energy calibration was performed with C1s 284.8 eV.

2.3. Experiment

When the sample is in a steady state, the heat flux is constant in any part, i.e., the one-dimensional steady-state thermal conductivity is without an internal heat source, and the condensing surface temperature is calculated using the one-dimensional Fourier's heat transfer law. Based on the one-dimensional heat transfer law, the surface temperature of the sample is derived from the internal temperature of the sample as follows.

$$T_W = T_i + \frac{Q \times \Delta l}{A \times \lambda} \tag{1}$$

$$Q = \frac{M \times H_{fg}}{t} \tag{2}$$

where T_i is the temperature of the back side of the condensing surface (K), Δl is the distance from the temperature measurement point to the condensing surface (m), and λ is the thermal conductivity of the condensing sample (W·m^{-1}·K^{-1}). Q is the heat conductivity of the condensing surface of the specimen (W), A is the effective heat transfer area of the condensing specimen (m^2), M is the mass of condensate (kg), and H_{fg} is the latent heat of vaporization of condensate (J/kg).

According to the heat transfer theory, the heat transfer coefficient h is obtained.

$$h = \frac{Q}{A \times \Delta T} = \frac{Q}{A \times (T_S - T_W)} \tag{3}$$

where T is the condensation time (s), T_S is the vapor temperature (K), and T_W is the surface temperature of the condensing specimen (K).

Figure 1 illustrates a schematic diagram of the condensation experiment device. The experiments were carried out at atmospheric pressure, with a temperature of $21 \pm 0.5\,°C$, relative humidity of $75 \pm 1\%$, a cooling water temperature of $16 \pm 0.1\,°C$, a steam temperature of $90 \pm 2\,°C$, a steam pressure of 0.1 MPa, and a steam flow rate of 200 cm^3/min. The temperature measuring module measured the experimental temperature on the back of the condensed sample, and the data acquisition error was less than 1%. Condensation heat transfer tests were performed using the three different SiC samples mentioned above. Two sets of control experiments were conducted in order to prevent errors in the experimental results, and the average of the two sets of data was taken as the experimental results. The same temperature and humidity were used for all of the condensation heat transfer tests. After measuring the sample's backside temperature and the condensate's weight, the condensation surface temperature and heat transfer quantity were calculated using Equations (1) and (2), respectively. Lastly, Equation (3) was used to get the sample's condensation heat transfer coefficient.
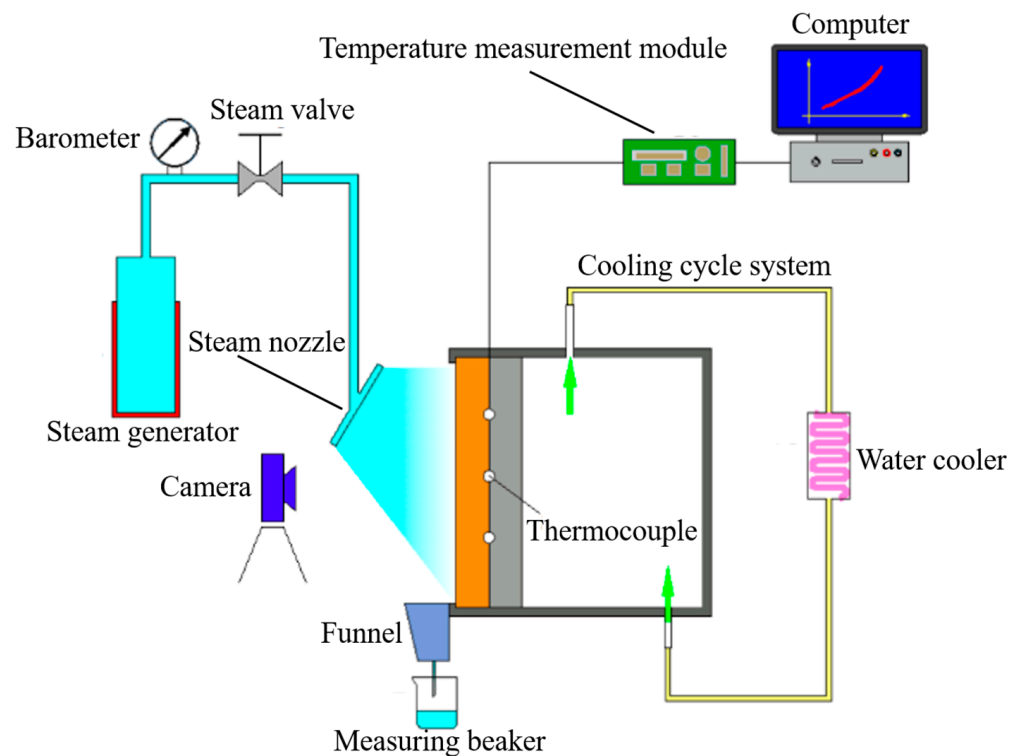
Figure 1. Schematic diagram of the condensation experiment device.

3. Results and Discussion

3.1. Effect of Laser Texturing and Heat Treatment on Microstructure and Composition

Figure 2 shows the contact angles of three SiC surfaces measured by the contact angle measuring instrument. Figure 2a shows that the contact angle of the original sample is $71 \pm 1.8°$. Figure 2b shows that the contact angle of the LT sample is at 0° (superhydrophilic). Figure 2c shows that the contact angle of the LT and HT sample is at $164 \pm 1.5°$ (superhydrophobic).

Figure 2. The contact angles of the three surfaces: (**a**) the original sample, (**b**) the LT sample, (**c**) LT and HT samples.

Figure 3 shows SEM images of the three surfaces. Figure 3a shows the original SiC surface after grinding, with a relatively rough surface and extensive distribution of grooves. Additionally, from Figure 3a–c, it is clear that both LT and LT and HT samples reserve most of the grain boundary and grooves from the original. However, Figure 3b is the LT surface with obvious traces of laser action, which has removed the capture of free organic matter from the original surface and presents a superhydrophilic (SHPi) state. It shows the micron-sized bump structure on the LT surface, with several small nanoscale particles adhering to the top of the bump. The LT surface has less nano-burr structure, and the droplet has a large contact area with the surface, so the surface shows SHPi. Figure 3c shows the nanoscale sheet-like protrusion structure on the LT and HT surfaces. After heat treatment, the small nanoparticles attached to the tabs grew sufficiently to form protrusions. As the droplet had a small contact area with the surface, the LT and HT surface shows SHPo. When the droplet came in contact with the surface, it gradually filled the entire nano groove. If the driving force of the droplet exceeded the hysteresis resistance, the bottom radius of the droplet began to contract. Among them, the nanostructure of the LT and HT surface formed multiple air pockets in contact with air. When the bottom radius shrank to a certain extent, the percentage of contact area between the droplets and the surface decreased, and most of the droplets were lifted by this air film. This indicated that the nanostructure of the LT and HT surface could effectively capture air, reduce the contact area between droplets and the surface, and play a decisive role in the generation of superhydrophobicity.

Figure 4 shows the three-dimensional surface profile of the samples. Figure 4a shows the LT sample surface, where after laser processing of the sample surface, fewer nano-burr structures are formed on the sample surface, and the droplets have a large contact area with the surface, showing the SHPi state. Figure 4b shows the LT and HT surface, where the surface forms a nanoscale sheet-like protrusion structure, and it shows SHPo. The surface roughness of the sample was increased from 0.21 μm to 5.58 μm after laser processing and heat treatment; thus, the SiC surface changed from superhydrophilic to superhydrophobic.
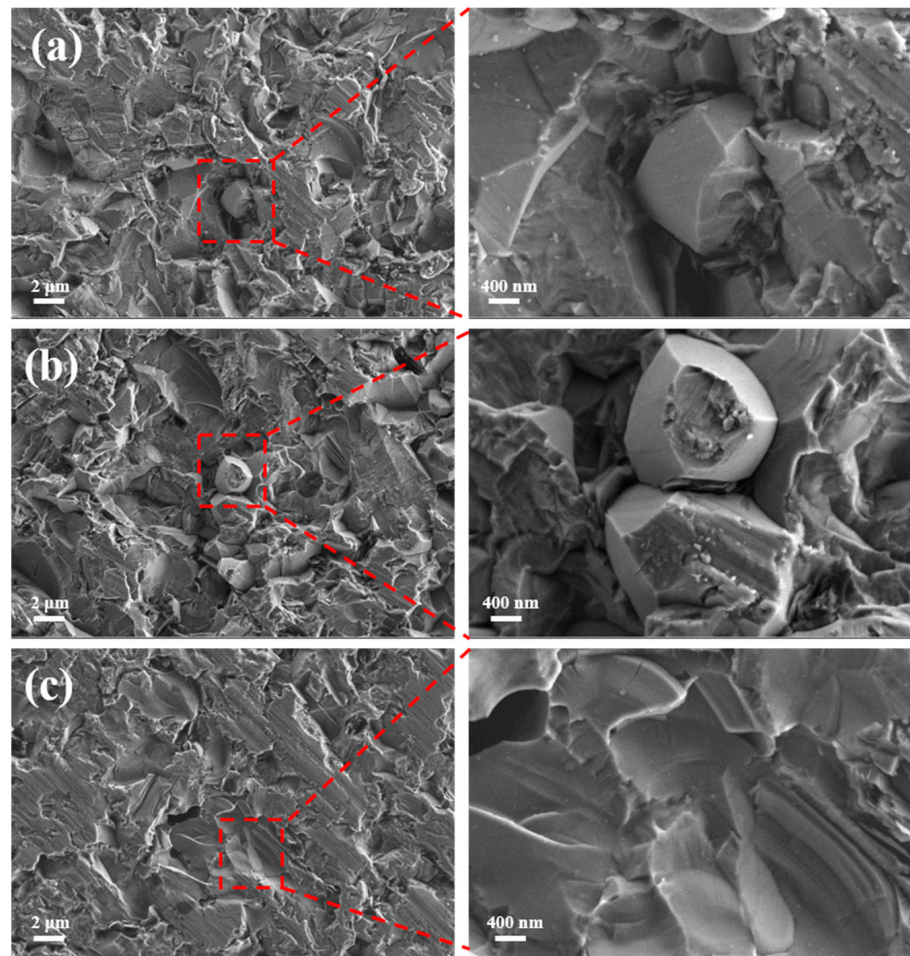
Figure 3. SEM images of the three surfaces: (**a**) original, (**b**) LT sample, (**c**) LT and HT sample.
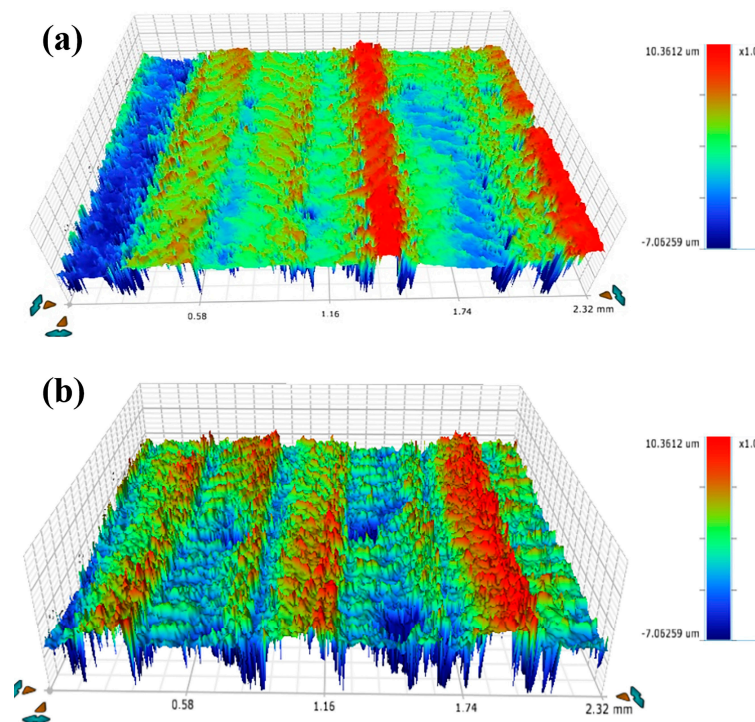
Figure 4. The three-dimensional surface profile of the samples: (**a**) LT sample; (**b**) LT and HT sample.

Figure 5 shows the atomic content of the samples. The percentage of oxygen elements on the original surface, the LT surface, and the LT and HT surface are 17.07%, 46.79%, and 48.04%, respectively. Meanwhile, the percentage of elemental carbon on the original surface, the LT surface, and the LT and HT surface are 42.72%, 19.53%, and 10.71%, respectively. During the laser texturing process, the SiC surface reacted with oxygen to form SiO_2, and the free organic matter adsorbed on the original surface was removed. After the SiC samples were baked at high temperatures, some SiO on the SiC surface continued to oxidize to SiO_2, and therefore the oxygen content increased.
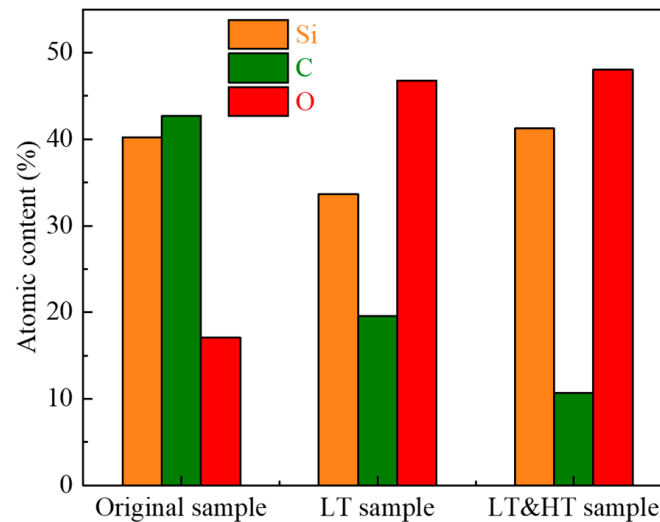

Figure 5. The atomic content of the samples.

Figure 6 shows the XPS characteristic spectral lines of the three surfaces. Figure 6a–c shows the XPS analysis of three different SiC surfaces. According to the Si2p spectrum of SiC samples, it can be known that the peaks of 100.5 eV, 102.2 eV, and 104.1 eV belong to SiC, SiO_X, and SiO_2, respectively. The SiC content and SiO_X content of the original surface are 97.3 wt.% and 2.7 wt.%, respectively. The SiC interface reacted with the surroundings during LT, and the SiC content is not obvious. The contents of SiO_X and SiO_2 on the surface are 34.51 wt.% and 65.49 wt.%, respectively. The possible reaction [24–27] was: $2SiC + 2O_2 \rightarrow SiO_X$ (s) $+ SiO_2 + CO$. At the same time, the surface-captured free organic matter was removed, and SiO_2 surface energy was relatively high, so the surface was in a SHPi state. After LT and HT, SiC content was not obvious, SiO_X content increased to 69.76 wt.%, and SiO_2 content was 30.24 wt.%. During heat treatment, the nano-groove structure was formed, and the low surface energy SiO_X produced on the surface, the surface became SHPo.
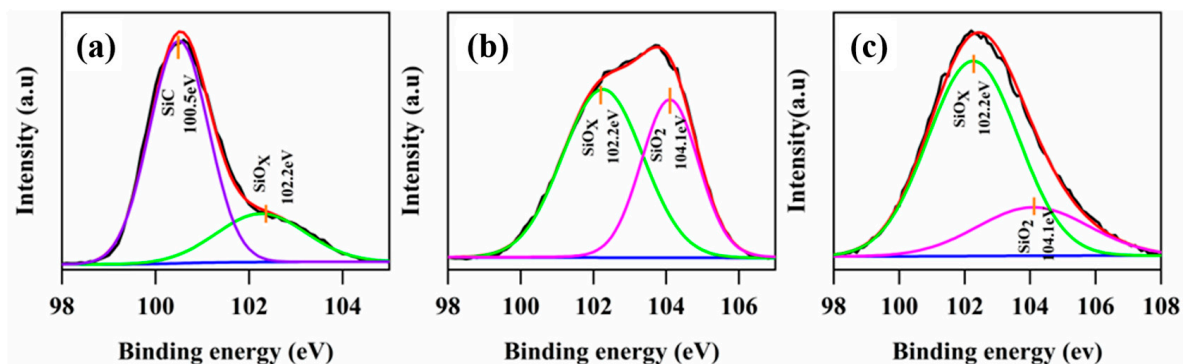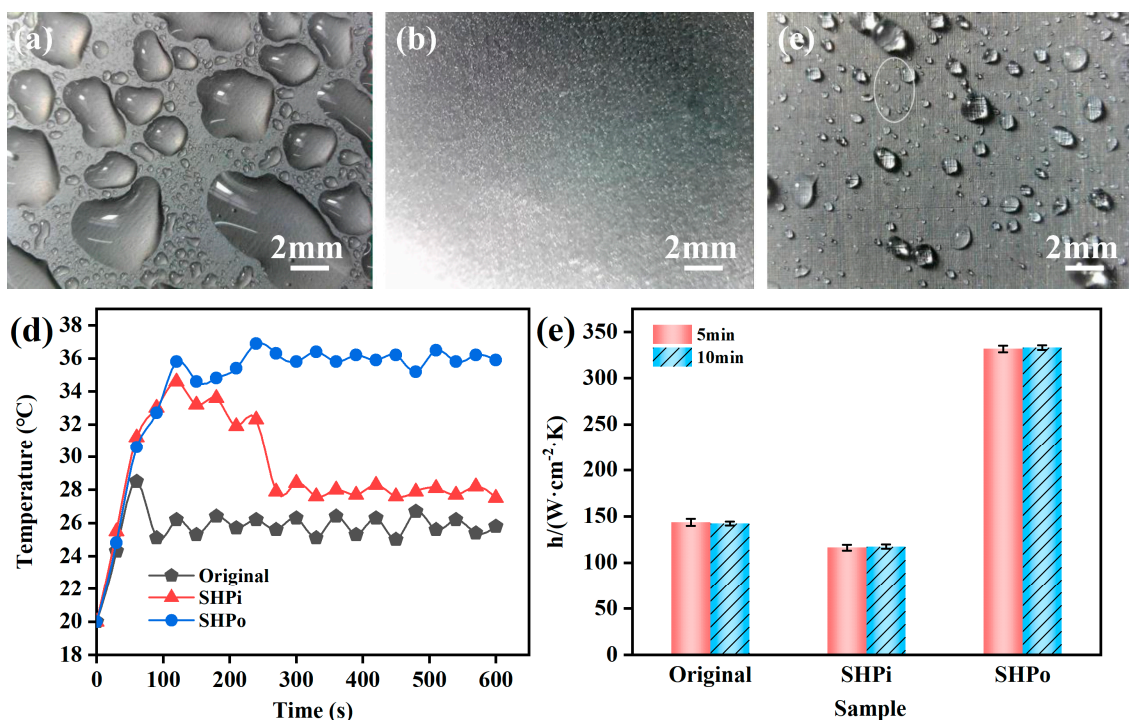

Figure 6. XPS spectra of 3 SiC surfaces: (**a**) original sample; (**b**) LT sample; (**c**) LT and HT sample.

3.2. Condensation Heat Transfer

Figure 7 shows the steam condensation images and heat transfer performance of three different SiC surfaces. Figure 7a shows the steam condensation image on the original surface, the transitional condensation from filmwise to dropwise is obvious. Figure 7b shows the steam condensation image on the LT surface, and it can be seen that the vapor continuously attached to the SHPi surface and became liquid, formed a liquid film, and then started to flow, which is the filmwise condensation. Figure 7c shows the steam condensation image on the LT and HT surface; it can be seen that the vapor slowly attached to the superhydrophobic surface and formed small droplets. As the condensation process continued, the small droplet slowly grew, and the neighboring droplets adsorbed each other under the action of surface tension so that the neighboring droplets slowly came together, merging and pooling between the neighboring droplets. When the gravity of the droplet is less than the surface adhesion force, the droplet will form. When the gravity of the droplet is greater than the surface adhesion force, the droplet will shed and, at the same time, take the tiny droplet being formed with it, providing more space for the small droplet to form on the surface. This is dropwise condensation.

Figure 7. Condensation images and heat transfer performances of 3 SiC surfaces: (**a**) original; (**b**) LT SHPi; (**c**) LT and HT SHPo; (**d**) T–t curves; (**e**) heat transfer coefficients.

During dropwise condensation, the vapor slowly adheres and forms small droplets on the SiC surface. Because the diameter of the newly formed droplets is smaller than the spacing of the micro-nano multilevel structure on the SiC surface, the droplets form tiny droplets in the multilevel structure grooves at the beginning of the condensation experiment, and the position of the tiny droplets formed on the superhydrophobic surface is not fixed because the droplet nucleation on the surface is random. When the vapor continues to connect to the SiC SHPo surface, the droplets continue to grow, and because the two droplets are still far apart, the SiC superhydrophobic surface is covered with fewer small droplets, and the adjacent droplets have not yet merged. With the continuous growth of condensed droplets, the distance between the two droplets becomes smaller and smaller to the droplet merger under the action of surface tension small. When the size of the merged droplets is larger than the distance between the surface micro-nano

structures, there will be a merging of droplets at the upper end of the two raised structures. Between the merged micro-nano grooves, the liquid forms a closed-air film between the upper end of the projection and the grooves due to the presence of air inside the grooves. While vapor condensation continues, the droplets will continue to increase in size, but the droplets above the air film are held up due to the presence of the air film between the grooves, at which time the contact area between the droplets and the surface decreases, and the droplets continue to grow and merge. When the distance between the micro-nano structures on the surface is larger than the size of the droplets after merging, the tiny droplets nucleated inside the grooves will keep growing, and when the droplets grow large enough, the droplets at the upper end of the grooves are attracted to the lower part by the droplet tension inside the droplets, and the merging between the droplets will occur inside the grooves. As the water vapor condensation continues, the droplets will gradually fill the grooves between the micro-nano structures, thus making the droplets present on the SiC surface. As the water vapor condensation continues, the droplets gradually fill the grooves between the micro-nano structures, thus making the droplets assume a super hydrophilic state on the SiC surface, forming a liquid film that prevents the vapor from continuing to nucleate.

As seen in Figure 7d, during the 120 s condensation test, the SHPo and SHPi surface temperatures steadily increased with the same rising trend. During the 120 s–600 s condensation process, the SHPo surface temperature reaches a maximum value (about 36 °C) and then tends to stabilize, while the SHPi surface temperature reaches a maximum value and then suddenly drops to a certain temperature value (about 28 °C). The original surface temperature reaches a stable value (about 26 °C) around 80 s and remains stable. After 10 min of testing, the SHPo SiC surface temperature was the highest, the original was the lowest, and the SHPi one was in the middle. At the beginning of the test, the temperature of the three surfaces gradually increased, and the rising trend was consistent. After that, the temperature of the SHPo surface reached the maximum value and then stabilized; the original soon remained stable. The SHPi surface, on the other hand, decreased and remained stable after reaching its maximum value. The droplets did not completely fill the grooves at the beginning of the experiment. As the condensation proceeded, the surface was gradually wetted by droplets, and the condensation form gradually changed to filmwise condensation; thus, its surface temperature dropped abruptly. The droplets condensed rapidly on the SHPo surface, and when the droplets grew and merged to reach the droplet shedding diameter, the droplets would fall off from the SiC surface under the action of gravity. At the same time, the small droplets that were still nucleated would be detached together. These new condensation areas provided more areas for vapor condensation on the surface, thus making the mass of condensing droplets increase per unit of time, and the condensation heat transfer efficiency was high. As the condensation of steam continues, the droplets inside the grooves between the micro-nano structures will slowly increase, and their surface tension will adsorb the condensate droplets on the raised structures, and the condensate droplets will gradually fill the grooves, thus forming a liquid film on the condensing surface. As the condensate increases, the liquid film will gradually thicken, organizing the droplets from the gaseous state to the liquid state, making the condensation form into filmwise condensation, and the heat transfer efficiency decreases significantly.

Figure 7e shows the condensation heat transfer coefficients of three different SiC samples. The maximum condensation heat transfer coefficient of the SHPo surface is 331.8 ± 2.1 W/(m^2·K), which is 2.3 times the original and 2.8 times the SHPi. The condensation heat transfer coefficient of the SHPi surface is smaller because, during the condensation process, the SHPi surface undergoes filmwise condensation. In this state, the heat released from steam condensation could only be transferred to the surface through the liquid film. Therefore, the surface thermal resistance was high, and the condensation heat transfer coefficient of the SHPi surface was small. The condensation heat transfer coefficient of the SHPo surface was larger because dropwise condensation occurs on the SHPo surface

during the condensation process. The nucleation density of the SHPo surface was small, the droplet shedding frequency was high, and it was difficult for the droplets to form into a film. Therefore, the heat released from steam condensation could be directly transferred to the wall, and the condensation heat transfer coefficient of the SHPo surface was larger. It can be seen that dropwise condensation on the SHPo surface can greatly improve the heat transfer efficiency of condensation.

4. Conclusions

In this study, the SHPo SiC surface was prepared through laser texturing and heat treatment, and the condensation heat transfer experiment was conducted. Through microstructure investigation and theoretical analysis, the conclusions are drawn as follows:

(1) After laser texturing, the micron-sized bump structure is formed on the LT surface, and the LT surface shows SHPi. After heat treatment, the small nanoparticles attached to the tabs grew sufficiently to form nanoscale sheet-like protrusion structures. Meanwhile, the surface roughness of the LT and HT sample was 27 times higher than that of the LT sample. Thus, the LT and HT surface shows SHPo, and the contact angle is at $164°$;

(2) During laser texturing, the SiC surface reacts with oxygen to form SiO_2 and cleans up the free organic matter adsorbed on the original surface to be SHPi. After heat treatment, lower surface energy SiO_X (s) are produced. Combined with the nano-groove structures, the LT and HT surface becomes SHPo;

(3) The SHPo SiC surface shows a typical dropwise condensation. The heat transfer coefficient reaches $331.8 \text{ W}/(\text{m}^2 \cdot \text{K})$, which is 2.3 times the original surface and 2.8 times the SHPi surface.

Author Contributions: Conceptualization, D.L. (Deyuan Lou) and D.L. (Dun Liu); methodology, D.L. (Deyuan Lou); validation, D.L. (Deyuan Lou); formal analysis, D.L. (Deyuan Lou), P.C., H.L., Q.T. and Q.Y.; investigation, D.L. (Deyuan Lou); resources, D.L. (Deyuan Lou), P.C. and Q.Y.; data curation, G.L., P.C. and Q.Y.; writing—original draft preparation, G.L.; writing—review and editing, D.L. (Deyuan Lou) and G.L.; visualization, D.L. (Deyuan Lou); supervision, D.L. (Deyuan Lou) and D.L. (Dun Liu); project administration, D.L. (Deyuan Lou); funding acquisition, D.L. (Deyuan Lou) and D.L. (Dun Liu). All authors have read and agreed to the published version of the manuscript.

Data Availability Statement: Not Applicable.

Conflicts of Interest: The authors declare no conflict of interest.

References

1. Li, X.; Wang, X.; Bondokov, R.; Morris, J.; An, Y.H.; Sudarshan, T.S. Micro/nanoscale mechanical and tribological characterization of SiC for orthopedic applications. *J. Biomed. Mater. Res. B Appl. Biomater.* **2005**, *72*, 353–361. [CrossRef] [PubMed]
2. Van Erp, R.; Soleimanzadeh, R.; Nela, L.; Kampitsis, G.; Matioli, E. Co-designing electronics with microfluidics for more sustainable cooling. *Nature* **2020**, *585*, 211–216. [CrossRef]
3. Ma, D.; Xiao, G.; Zhang, T.; Yang, F.; Zhu, M.; Yuan, T.; Ma, L.; Gan, Y.; Wang, L. A Highly Integrated Multichip SiC MOSFET Power Module With Optimized Electrical and Thermal Performances. *IEEE J. Emerg. Sel. Top. Power Electron.* **2022**, *11*, 1722–1736. [CrossRef]
4. Zhang, H.; Bai, H.; Peng, P.; Guo, W.; Zou, G.; Liu, L. SiC chip attachment sintered by nanosilver paste and their shear strength evaluation. *Weld. World* **2019**, *63*, 1055–1063. [CrossRef]
5. Chang, W.; Luo, K.; Wang, P.; Li, C. Sustaining dropwise condensation on nickel-plated copper surfaces with As-grown graphene coatings. *Appl. Therm. Eng.* **2022**, *209*, 118319. [CrossRef]
6. El Fil, B.; Kini, G.; Garimella, S. A review of dropwise condensation: Theory, modeling, experiments, and applications. *Int. J. Heat Mass Transf.* **2020**, *160*, 120172. [CrossRef]
7. Rose, J.W. Dropwise condensation theory and experiment: A review. *Proc. Inst. Mech. Eng. Part A2 J. Power Energy* **2002**, *216*, 115–128. [CrossRef]
8. Khatir, Z.; Kubiak, K.; Jimack, P.; Mathia, T. Dropwise condensation heat transfer process optimisation on superhydrophobic surfaces using a multi-disciplinary approach. *Appl. Therm. Eng.* **2016**, *106*, 1337–1344. [CrossRef]

9. Liu, Y.; Lin, W.; Lin, Z.; Xiu, Y.; Wong, C.P. A combined etching process toward robust superhydrophobic SiC surfaces. *Nanotechnology* **2012**, *23*, 255703. [CrossRef]
10. Yoon, S.-S.; Lee, Y.B.; Khang, D.-Y. Etchant wettability in bulk micromachining of Si by metal-assisted chemical etching. *Appl. Surf. Sci.* **2016**, *370*, 117–125. [CrossRef]
11. Chen, D.; Zhu, S.; Li, W.; Kang, Z. Stable superhydrophobic and conductive surface: Fabrication of interstitial coral-like copper nanostructure by self-assembly and spray deposition. *Colloids Surf. A Physicochem. Eng. Asp.* **2022**, *638*, 128299. [CrossRef]
12. Zhu, Z.; Tian, Y.; Liu, Y.; Fu, K.; Chen, Q.; Zhang, B.; Zhang, H.; Zhang, Q. Facile synthesis of superhydrophobic coating with icing delay ability by the self-assembly of PVDF clusters. *Colloids Surf. A Physicochem. Eng. Asp.* **2022**, *641*, 128562. [CrossRef]
13. Lv, Z.; Yu, S.; Song, K.; Zhou, X.; Yin, X. A two-step method fabricating a hierarchical leaf-like superamphiphobic PTFE/CuO coating on 6061Al. *Prog. Org. Coat.* **2020**, *147*, 105723. [CrossRef]
14. Khan, A.; Sohail, S.; Jacob, C. The fabrication of stable superhydrophobic surfaces using a thin Au/Pd coating over a hydrophilic 3C-SiC nanorod network. *Appl. Surf. Sci.* **2015**, *353*, 964–972. [CrossRef]
15. Preston, D.J.; Mafra, D.L.; Miljkovic, N.; Kong, J.; Wang, E.N. Scalable Graphene Coatings for Enhanced Condensation Heat Transfer. *Nano Lett.* **2015**, *15*, 2902–2909. [CrossRef]
16. Chen, Z.; Wu, C.; Zhou, H.; Zhang, G.; Yan, H. A high-efficiency preparation method of super wear-resistant superhydrophobic surface with hierarchical structure using wire electrical discharge machining. *Surf. Coat. Technol.* **2022**, *444*, 128673. [CrossRef]
17. Duarte, M.; Lasagni, A.; Giovanelli, R.; Narciso, J.; Louis, E.; Mücklich, F. Increasing Lubricant Film Lifetime by Grooving Periodical Patterns Using Laser Interference Metallurgy. *Adv. Eng. Mater.* **2008**, *10*, 554–558. [CrossRef]
18. Wang, Q.; Wang, H.; Zhu, Z.; Xiang, N.; Wang, Z.; Sun, G. Switchable wettability control of titanium via facile nanosecond laser-based surface texturing. *Surf. Interfaces* **2021**, *24*, 101122. [CrossRef]
19. Sataeva, N.E.; Boinovich, L.B.; Emelyanenko, K.A.; Domantovsky, A.G.; Emelyanenko, A.M. Laser-assisted processing of aluminum alloy for the fabrication of superhydrophobic coatings withstanding multiple degradation factors. *Surf. Coat. Technol.* **2020**, *397*, 125993. [CrossRef]
20. Liang, L.; Lu, L.; Xing, D.; Wan, Z.; Tang, Y. Preparation of superhydrophobic and anti-resin-adhesive surfaces with micro/nanoscale structures on high-speed steel via laser processing. *Surf. Coat. Technol.* **2018**, *357*, 57–68. [CrossRef]
21. Gu, Z.; Yang, Y.; Li, K.; Tao, X.; Eres, G.; Howe, J.Y.; Zhang, L.; Li, X.; Pan, Z. Aligned carbon nanotube-reinforced silicon carbide composites produced by chemical vapor infiltration. *Carbon* **2011**, *49*, 2475–2482. [CrossRef]
22. Laurent, V.; Chatain, D.; Eustathopoulos, N. Wettability of SiC by aluminium and Al-Si alloys. *J. Mater. Sci.* **1987**, *22*, 244–250. [CrossRef]
23. Hong, Z.; Jiang, H.; Xue, M.; Ke, C.; Luo, Y.; Yin, Z.; Xie, C.; Zhang, F.; Xing, Y. SiC-enhanced polyurethane composite coatings with excellent anti-fouling, mechanical, thermal, chemical properties on various substrates. *Prog. Org. Coat.* **2022**, *168*, 106909. [CrossRef]
24. Caccia, M.; Giuranno, D.; Molina-Jorda, J.M.; Moral, M.; Nowak, R.; Ricci, E.; Sobczak, N.; Narciso, J.; Sanz, J.F. Graphene Translucency and Interfacial Interactions in the Gold/Graphene/SiC System. *J. Phys. Chem. Lett.* **2018**, *9*, 3850–3855. [CrossRef]
25. Narciso, J.; García-Cordovilla, C.; Louis, E. Reactivity of thermally oxidized and unoxidized SiC particulates with aluminium-silicon alloys. *Mater. Sci. Eng. B* **1992**, *15*, 148–155. [CrossRef]
26. Deng, Y.; Zhou, Y.; Zhang, Y.; Chen, D.; Zhou, X. Numerical and experimental analysis of nanosecond laser ablation of SiC. *Mater. Sci. Semicond. Process.* **2022**, *151*, 107020. [CrossRef]
27. Huang, Y.; Tang, F.; Guo, Z.; Wang, X. Accelerated ICP etching of 6H-SiC by femtosecond laser modification. *Appl. Surf. Sci.* **2019**, *488*, 853–864. [CrossRef]